Compare Results

Old File:

fdem_old.pdf

20 pages (3.72 MB)

5/10/2022 1:20:49 PM

versus

New File:

developing_lowcost_fdem_instrument_5142022.pdf

21 pages (3.54 MB)

5/13/2022 11:09:17 PM

Total Changes

403

Content

139 Replacements

127 Insertions

101 Deletions

Styling and Annotations

14 Styling

22 Annotations

Go to First Change (page 1)

Developing a low-cost frequency-domain electromagnetic induction instrument

Gavin Wilson[1], Jacob Conrad[1], John Anderson[1], Andrei Swidinsky[1,2], and Jeffrey Shragge[1]

[1]Department of Geophysics, Colorado School of Mines, Golden, CO, United States
[2]Now at Department of Earth Sciences, University of Toronto, Toronto, ON, Canada

Correspondence: Gavin Wilson (gswilson@mines.edu)

Abstract. Recent advancements and the widespread availability of low-cost microcontrollers and electronic components have created new opportunities for developing and using low-cost, open-source instrumentation for near-surface geophysical investigations. Geophysical methods that do not require ground contact, such as frequency-domain electromagnetics, allow one or two users to quickly acquire significant amounts of ground resistivity data in a cost-effective manner. The Colorado School of Mines electromagnetic system (CSM-EM) is a proof-of-concept instrument capable of sensing conductive objects in near-surface environments, and is similar in concept to commercial grade equipment while costing under US$400 to build. We tested the functionality of the CSM-EM system in a controlled laboratory setting during the design phase and validated it over a conductive target in an outdoor environment. The transmitter antenna can generate a current of over 2.5 A, and emit signals that are detectable by a receiver antenna at offsets of up to 25 m. The system requires little refitting to change the functioning frequency, and has been operationally validated at 0.4 kHz and 1.6 kHz. The receiver signal can be measured by off-the-shelf digital multimeters. Future directions will focus on improving the electronic and mechanical stability of the CSM-EM with the goal of using acquired data to make quantitative measurements of subsurface resistivity.

1 Introduction

Near-surface geophysical surveying using electrical and electromagnetic (EM) methods has experienced growth in recent years due to increased interest in identifying groundwater resources (Boaga, 2017), addressing environmental remediation concerns (White et al., 2016), and performing archaeological reconnaissance studies (Sea and Ernenwein, 2020). These near-surface geophysical techniques provide non-invasive and cost-effective approaches for imaging subsurface structures and estimating earth properties, compared to direct methods such as drilling or excavation (Ward and Hohmann, 1988). Additional near-surface EM application examples include using resistivity data combined with soil sampling and satellite imagery to develop frameworks for farm irrigation management (Fontaine et al., 2018); applying EM methods for environmental remediation to assess the location and areal extent of pollutants including landfills and radioactive waste disposal sites (White et al., 2016); and developing light-weight drone-based EM systems for detecting and classifying unexploded ordinance (Shubitidze et al., 2021), which opens up opportunities for drone-based EM surveying in environmental and agricultural applications.

While geophysical methods can assist with subsurface investigations, the cost of commercial instruments required to perform such surveys can be prohibitively expensive and effectively form a "barrier to entry" for many potential users. The price constraints of many commercial grade instruments stem from their hardware being designed for large-scale campaigns, industrial applications, and the capability to acquire high-quality data under extreme climate conditions (e.g., from the frozen Arctic to the hot desert). This leads to scenarios where commercial instruments are effectively "over-engineered" for many near-surface geophysical applications, when more elementary instrumentation and data acquisition procedures would suffice.

The recent rapid growth of low-cost microcontrollers (e.g., Arduino and Raspberry Pi) and sensors as well as the proliferation of open-source software packages allow entry-level and expert practitioners alike to build high-accuracy sensor systems within a price range affordable for small-scale research and enthusiast projects. These tools have the potential to be leveraged in purpose-built low-cost geophysical equipment that can acquire data without exceeding the durability and budgetary constraints for many types of near-surface geophysical investigations. Examples following this low-cost instrumentation approach include direct-current (DC) resistivity (Clark et al.; Ahmad et al., 2019; Sirota et al., 2021), seismic nodes (Dean et al., 2017; Soler-Llorens et al., 2019; Wilson et al., 2021), and magnetometers (Schofield et al., 2012; Shahsavani, 2018), each of which has demonstrated the possibility of acquiring data of comparable quality to commercial-grade systems. While such home-grown instrumentation is neither as robust nor as likely to have fully in-built safety factors as commercial grade instruments, it can lower the barrier-to-entry for many users, enable enthusiast, academic, or humanitarian geoscience applications, and be used to develop low-cost geophysical networks for time-lapse monitoring projects.

Frequency-domain electromagnetic methods (FDEM) represent a class of geophysical techniques that are important for near-surface applications due to their sensitivity to subsurface variations in electrical resistivity (or its inverse, electrical conductivity) due to, e.g., heterogeneity in geological material or variable fluid saturations. FDEM surveying is based on the principle of EM induction and requires only one or two operators to acquire data, meaning that the instrument need not be attached to the earth unlike grounded methods (e.g., DC resistivity, induced polarization, and seismic). This advantage allows users to acquire spatial FDEM geophysical data at greater rates than comparable ground-coupled methods, and furthermore makes the approach a strong candidate for EM drone-receiver based investigations. Overall, developing a low-cost FDEM system prototype that provides accurate data could create significant opportunities for numerous near-surface geophysical applications.

The primary goal of this study is to design, build, and validate a low-cost transmitter-receiver FDEM system for under US$400. Our developed proof-of-concept instrument, the CSM-EM, is of comparable size and transmits similar signal strength to the commercially available Geonics EM-34 system, and can detect conductive objects using amplitude-based signal measurements via an autoranging digital multimeter (DMM). The instrument is straightforward to operate and can function at a variety of transmitter/receiver frequencies with minimal refitting. The paper starts by briefly describing the theory behind the FDEM method and its use in geophysical investigations. We then discuss our low-cost FDEM transmitter-receiver system design and provide details on its construction. We conclude by presenting validation results for the system prototype in both laboratory and outdoor conditions, and by discussing the cost breakdown and future refinements of the device, along with possible applications in near-surface geophysical investigations.

2 Methods

The purpose of this section is to provide a brief review of the theoretical principles and some methodological considerations behind the FDEM technique. Readers interested in a more complete theoretical treatment are referred to standard reference texts on these subjects (Purcell, 1966; Ward and Hohmann, 1988).

2.1 FDEM Theory Overview

Electromagnetic methods measure ground resistivity through EM induction with separated transmitter (Tx) and receiver (Rx) antennas, allowing data acquisition without the need for ground contact. As detailed in the Instrument Design section below, the two antennas are circular coils of wire connected to different electronic modules. FDEM methods are based upon the principles of Ampere's and Faraday's Laws in a quasi-static regime, where an alternating current (AC) produces a magnetic field and an alternating magnetic field produces an electric field, respectively. As illustrated in Figure 1, FDEM uses a known and calibrated time-varying current in the Tx coil (blue loop) to produce an alternating primary magnetic field that is present in both the air and subsurface (solid gray lines). This field operates at a single frequency specified by the user. For scenarios involving conductive subsurface material, this alternating magnetic field will induce alternating eddy currents (orange lines) via Faraday's Law and Ohm's Law. As described by Ampere's Law, these eddy currents produce a secondary magnetic field (dashed black lines). The superimposed fields produce a time-varying current in the Rx coil (red loop), as per Faraday's Law. This signal will oscillate at the same frequency as the field generated by the Tx and can be measured as a voltage drop across a capacitor attached in series with the Rx antenna coil.

When the system is over a uniform halfspace of a given resistivity, a Tx-Rx configuration with a fixed offset and orientation will measure a constant voltage independent of lateral position. However, the presence of lateral subsurface heterogeneity will affect the signal detected by the Rx and introduce spatial dependence in the voltage measurements. This makes FDEM particularly effective at identifying lateral changes in soil-water content and at locating anomalous conductive bodies (such the conductive ellipsoid illustrated in Figure 1). Some commercial EM systems also use a tuneable third "bucking" coil to remove the primary field response from the Rx coil, due to the large amplitude of the primary field compared to that of the secondary field (the latter of which contains the relevant information about ground resistivity).

2.2 Penetration Depth

The penetration depth of any EM method is dependent upon a variety of subsurface physical properties as well as the frequency of the inducing magnetic field produced by the Tx. For FDEM field applications, the effect of these properties can be quantified using a proxy value known as the skin depth δ

$$\delta = \sqrt{\frac{\rho}{\pi \mu f}} \tag{1}$$

which represents the depth in the subsurface at which the field strength has decayed to $1/e$ (37%) of the surface value. Skin depth is dependent upon the subsurface electrical resistivity ρ, magnetic permeability μ, and the instrument operating frequency,
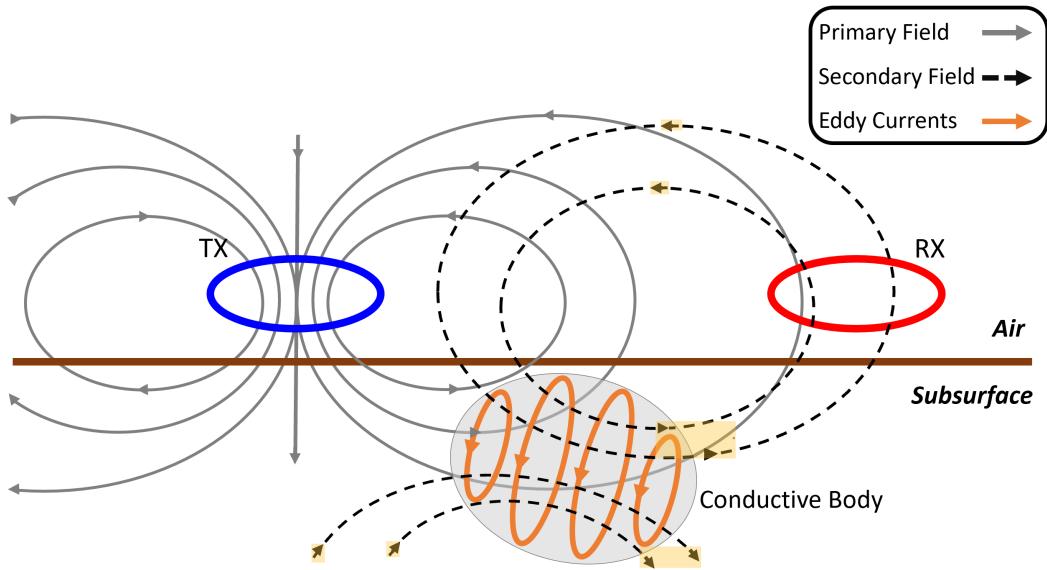
Figure 1. The magnetic fields resulting from a horizontal coplanar Tx-Rx system configuration over a conductive body. The Tx electronics produce a time-varying current in the Tx coil (blue ring), which generates an alternating magnetic field (solid gray line) that is present in the air and subsurface. This field will generate eddy currents in conductive subsurface material (orange lines) that create a secondary magnetic field (black dashed lines). The Rx unit (red ring) measures the combined effects of the time-varying primary and secondary magnetic fields as a voltage.

f. Electrical resistivity is related directly to subsurface geological structure, as well as any fluids that might be saturating the associated pore space. In most near-surface geological situations, the magnetic permeability μ can be assumed to equal the magnetic permeability of free space $\mu_0 = 4\pi \cdot 10^{-7}$ H/m. This means that we can increase or decrease the depth of investigation by changing the functioning frequency of the instrument.

While the frequency of the EM system can be used to alter the penetration depth of the inducing fields, different relative orientations of the Tx and Rx coils can be used to change the EM field radiation patterns and achieve different subsurface sensitivities. Figure 2 illustrates three common Tx-Rx "fully coupled" orientations, with the horizontal coplanar (HCP) being the most common investigation setup and the one used in the validation tests reported herein.

The Tx-Rx offset r has a significant effect on signal decay. For a uniform halfspace of resistivity ρ and an HCP configuration, the signal of frequency f is related to the vertical magnetic field strength detected by the Rx coil (Ward and Hohmann, 1988, Eq. 4.56). Changes in the vertical magnetic field can be measured as a voltage V_R by the Rx. This value is related to offset r by the general equation:

$$V_R = \frac{if\mu_0 A_T A_R N_T N_R I_T}{k^2 r^5}\left[9 - (9 + 9ikr - 4k^2r^2 + -ik^3r^3)e^{-ikr}\right],\tag{2}$$
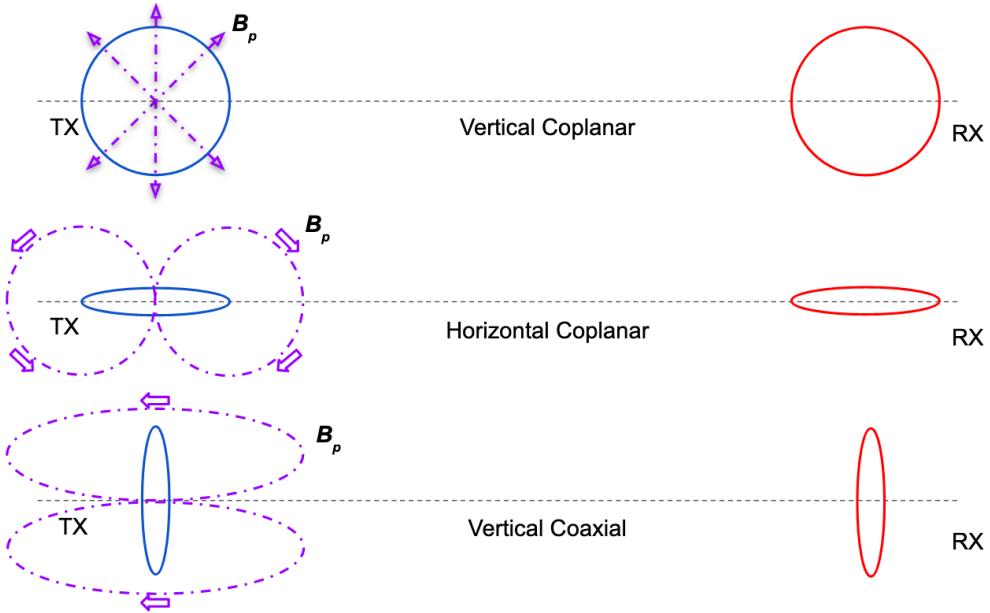
Figure 2. Fully coupled orientations for coplanar/coaxial Tx and Rx loops. The purple lines and arrows represent the magnetic field generated by the Tx antenna. Top: vertical coplanar. Middle: horizontal coplanar. Bottom: vertical coaxial.

where $k = \sqrt{\frac{-i\mu_0 2\pi f}{\rho}}$, I_T is the Tx current, and A_T, A_R, N_T, and N_R respectively are the areas and the number of wire turns around the Tx and Rx antennas. This equation is valid for both near field and far field situations. While f, k, and r solely account for the magnetic field strength at the Rx coil in an HCP Tx-Rx orientation, I_T, A_T, A_R, N_T, and N_R (Tx/Rx component parameters) affect the magnetic field strength and the value measured across Rx by a DMM. In this setting, μ_0 represents the permittivity of free space.

2.3 Instrument Sensitivity

The choice of component parameters (i.e., the effective areas of the Tx and Rx antennas) were based on the dimensions of the EM-34 conductivity meter due to its in-house availability and large size. Before building the prototype, the antenna parameters were tested by modeling the Rx voltage over a range of half-space resistivity values using a Python script to determine whether the CSM-EM range and resolution (0.1 mV-9.0 V) allowed the instrument to delineate between different geologic environments. This testing modeled the variation in Rx signal, which measures the time rate of change of the total vertical magnetic field, over a half space as a function of Tx-Rx offset (Figure 3a). We also examined how the secondary field, containing the information related to ground resistivity, changed with variable resistivity for a range of Tx-Rx offsets (Figure 3b). The total field voltage response modeling (i.e., the value measured by the instrument) shows that signals over different half-space resistivity values fall within CSM-EM resolution for most offsets from 1 m to 50 m. The only half-space resistivity falling outside the CSM-EM resolution was the simulated perfect conductor ($\rho = 10^{-6}$ Ω·m). By considering a

perfect resistor ($\rho = 10^6$ Ω·m), which shows a similar voltage response to that of the primary field, we observed that most realistic ground resistivities have a minute effect on the voltage response of the device. This exercise demonstrated that the

120   effect of the secondary field is difficult to detect for most half-space resistivities in the presence of the primary field. The secondary field response, however, showed that different half-space resistivities can be determined given the resolution of the CSM-EM system. While this can only be observed on the 1 Ω·m curve, other half-space curves show the same sign reversal response at larger offsets. The secondary field was calculated by subtracting the primary (free space) field from the total field. This calculation showed that subsurface resistivity variations ranging from 10^0 Ω·m to 10^2 Ω·m would be detectable within

125   the CSM-EM resolution at most Tx-Rx offsets. However, more resistive environments (e.g., 10^3 Ω·m) would generate an insufficient secondary field to create a voltage change detectable by the CSM-EM, given that most DMMs measure voltages to within a ±0.1 mV precision. The dip shown at 42 m on 1 Ω·m curve (Figure 3b) is due to a sign reversal of the signal, where the difference between the primary and total field amplitudes is at a minimum. This event can be observed in Figure 3a at 42 m as the 1 Ω·m curve intersects the perfect resistor voltage response curve.
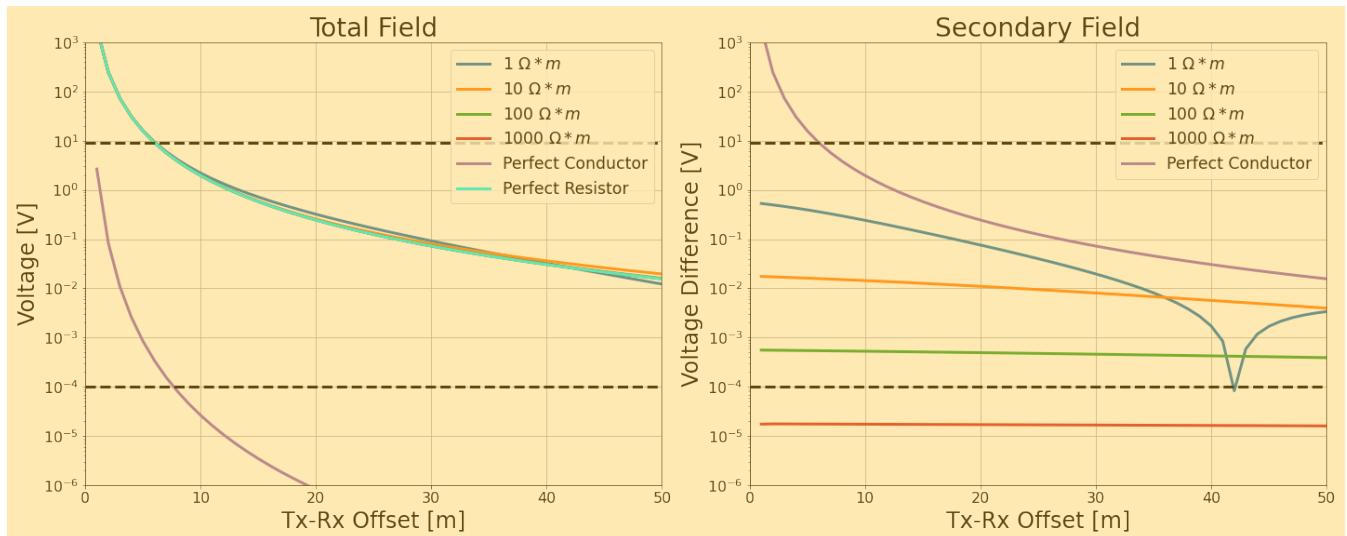
Figure 3. (a) The absolute value of the Rx voltage measured by a horizontal coplanar (HCP) configuration, corresponding to the change in the total vertical magnetic field, resting on a halfspace of variable conductivity as a function of Tx-Rx offset. All Rx electronic parameters (resistance, inductance, capacitance, amplifier gain) are as indicated in Figure 4, with a Tx frequency of 1680 Hz, a current of 2.0 A, and Tx and Rx coil areas of 0.29 m^2 each with 100 turns. The dashed horizontal lines indicate the upper (9.0 V) and lower (0.1 mV) limits of the Rx amplifier power supply and DMM resolution, respectively. (b) Difference between free-air and half-space voltages (effectively the amplitude change of the secondary field) for an HCP configuration with all parameters identical to those shown in (a).

3 Instrument Design

The primary goals in the design of the low-cost CSM-EM FDEM system are to: (1) construct an adaptable device able to function at multiple signal frequencies and Tx-Rx offsets similar to commercial FDEM instrumentation; (2) use basic and easily sourced electrical components; and (3) maintain a sub-$400 instrument build cost. While the use of low-cost components sacrifices some of the durability found in commercial systems, easily procurable components facilitate replacement or even the construction of multiple EM systems to work independently or jointly and allow capital expenditure.

The design goals for the low-cost CSM-EM device require that the Tx-Rx frequency can be adjusted with minor hardware changes and that the CSM-EM Tx signal is comparable in strength to that offered by a commercial FDEM system Tx.

3.1 Functionality & Workflow

The CSM-EM instrument is composed of independent Tx and Rx units. During data acquisition, the Tx hardware module generates an AC signal that is amplified and transmitted through the Tx antenna. Both the primary EM field from the Tx unit and secondary fields generated by conductive subsurface heterogeneity are measured by the Rx antenna. The composite signal is filtered and then amplified so that voltage changes can be sensed with a 0.1 mV resolution DMM (Figure 3 shows the system resolution limits) capable of measuring AC signals. The multimeter records an approximate root-mean-squared (RMS) voltage, which is a simple measure of the signal magnitude generated by the primary Tx field and any secondary EM fields. The design and functionality of the Tx and Rx units are described below. The specific component values represented in CSM-EM design can be easily modified and are based on the calibrated inductance and resistances of the Tx and Rx coils. The resistances of the coils were measured using a DMM (resistance setting). Coil inductances were measured by using a precision capacitor in series with the coil to create an RLC circuit, scanning through a range of input frequencies until achieving resonance in the coil, and finally back-solving for coil inductance (L_{coil}) using equation 5. By tailoring component values to the Tx and Rx properties, the CSM-EM can be constructed using easily substituted parts.

3.2 Transmitter Design

The series of hardware modules of the CSM-EM Tx unit and the circuitry design behind each module are presented in Figures 4a and 4b, respectively. The resistor-capacitor (RC) oscillator and power amplifier modules are powered by two 12 V motorcycle batteries. Alternatively, the system could be powered by four 12 V batteries with two pairs connected in series to obtain a larger Tx current; however, following this approach may shorten instrument longevity in the field.

The Tx system generates an AC signal using an RC oscillator module. An RC oscillator generates an AC signal using EM noise, RC circuit feedback, and signal amplification (see, for example, Alexander and Sadiku 2007). Any EM noise encountered by the module is filtered through several RC stages that introduce a phase shift at a given angle depending on the chosen RC component values and the number of stages N_S within the circuit. The cumulative RC signal conditioning creates a 180° phase shift. The resulting signal is subsequently amplified by an inverting operational amplifier, which causes another 180° phase shift. This shift creates regenerative feedback, allowing for a stronger AC signal to be generated solely
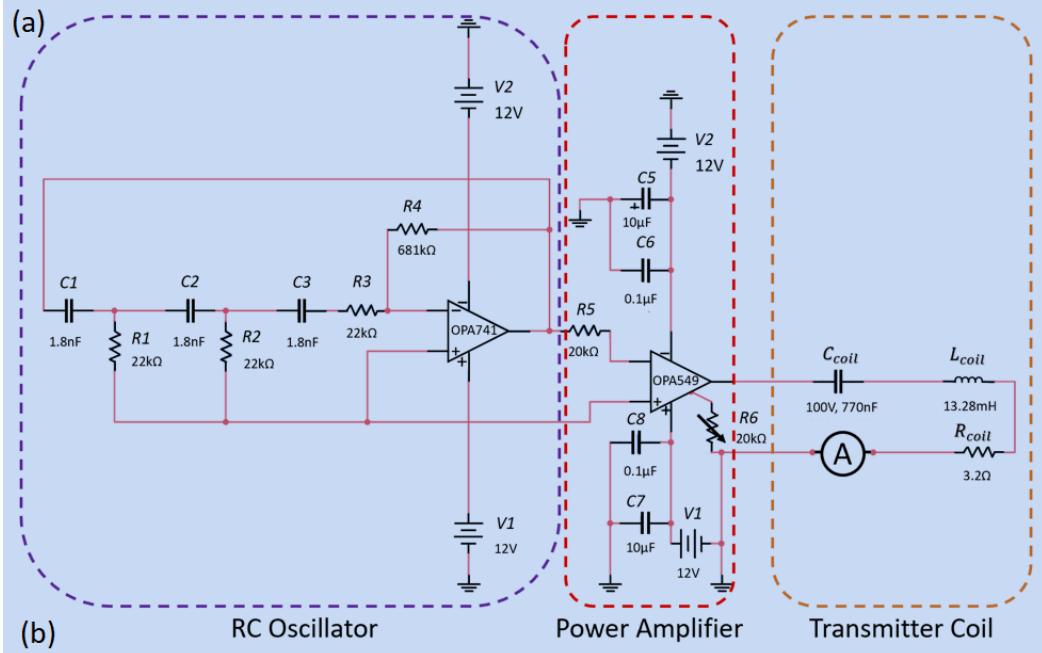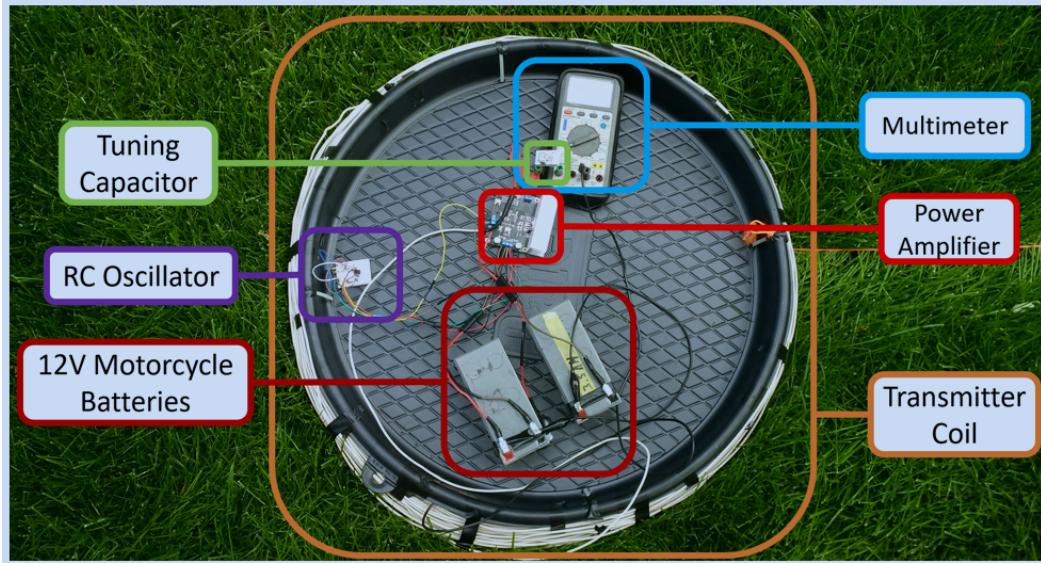
Figure 4. (a) Low-cost CSM-EM Tx system powered by two 12 V motorcycle batteries. The RC oscillator generates an AC signal at a given frequency, which is amplified by the power amplifier before being passed into the Tx coil to generate an AC signal and corresponding magnetic field. The DMM (ammeter setting) measures the alternating current passing through the 0.61 m diameter Tx coil. (b) CSM-EM Tx circuit diagram that can be split into three primary modules: the RC oscillator, the power/signal amplifier, and the Tx coil (with tuning capacitor). The circuit is composed of basic electronic components along with an OPA549 power amplifier breakout board. Resistor R_5 was included to allow sustained regenerative feedback in the circuit and is not part of a specific Tx module.

from ambient EM fields and a DC power source. The desired frequency f_{RC} (in Hz) of the AC signal can be calculated using

$$f_{RC} = \frac{1}{2\pi RC\sqrt{2N_S}}, \tag{3}$$

where R is resistance, C is capacitance, and N_S is the number of RC stages. The R and C components in each stage of the RC
oscillator must have the same respective resistance and capacitance values, meaning that in Figure 4b $R = R_1 = R_2 = R_3$ and
$C = C_1 = C_2 = C_3$. RC oscillators commonly have three RC stages to maintain signal stability (Alexander and Sadiku, 2007),
which is reflected in our CSM-EM oscillator module. Representative values of $C = 1.8$ nF, R = 22.0 kΩ, with $N_S = 3$ generate
an $f_{RC} = 1.64$ kHz. The output frequency of the CSM-EM system can be modified by switching out modular capacitor units
with differing C values and changing the tuning capacitor attached to the Tx antenna.

The stability of the signal output also depends on the applied amplifier gain. Gain is a unitless value that describes the ratio
between the voltage of the output signal from an operational amplifier (op-amp) to that of the input signal. The signal gain G
of the output voltage V_{out} is dependent on the values of resistors R_f and R attached to the op-amp and on the voltage of the
input signal V_{in}, as follows for a simple inverting amplifier:

$$V_{out} = GV_{in} = -V_{in}\left(\frac{R_f}{R}\right). \tag{4}$$

Figure 4b uses this setup within the RC oscillator assembly with a gain $G = 31$, which is controlled by resistors $R = R_3$ and
$R_f = R_4$ in Figure 4b. The op-amp gain of an RC oscillator must be $G \geq 29$ to main signal stability (Alexander and Sadiku,
2007); however, a value $G \gg 29$ tends to distort the AC signal.

The small AC signal generated by the RC oscillator is impractical at any field scale Tx-Rx offset (Alexander and Sadiku,
2007). The high-voltage, high-current op-amp device (OPA549) can supply a current up to 8.0 A to any load attached to
the output. The OPA549 has been driven to saturation as a ±12V square wave, the maximum signal gain allowable by the
power supplies, and does not follow equation 4. This specialized power amplifier is required for signal amplification needed to
generate measurable field-scale signals. The power amplifier is part of a pre-fabricated breakout board with DC power supply
regulating capacitors and a heat sink. We initially built a heat-sink attachment in-house (central unit in Figure 4b), but the
pre-fabricated unit (power amplifier in Figure 4a) proved to be safer, more durable, and reliable under field conditions.

Finally, the amplified signal is passed into the Tx antenna, consisting of 100 turns of 14 gauge wire around a 0.61 m (2 ft)
diameter coil. To generate resonance in the Tx coil at the same frequency as the RC oscillator, we must include a tuning
capacitor. The resulting RLC circuit uses a tuning capacitor C_{coil} and the inherent inductance L_{coil} of the Tx antenna to
provide an effective bandpass filter. The filtered output frequency f_{coil} is related to L_{coil} and C_{coil} via:

$$f_{coil} = \frac{1}{2\pi\sqrt{L_{coil}C_{coil}}}. \tag{5}$$

The Tx antenna had a measured inductance of $L_{coil} = 13.28$ mH that when combined with a $C_{coil} = 770$ nF tuning capacitor
created a bandpass filter with a peak frequency of $f_{coil} = 1.57$ kHz. The RLC circuit ensures that when the square-wave signal
passes through the Tx antenna, it is transmitted as a monochromatic sinusoidal wave. Although RLC filters theoretically pass
a single frequency, the Tx wire itself has a fixed resistance value; when combined with the RLC filter inductance L_{coil}, the

resistance R_{coil} dictates the filter pass-band width Δf_{width} (i.e., the frequency range about the peak value that is still passed through the filter). Whereas too broad of a pass band would weaken the resonance of the Tx antenna, too narrow of a pass band may decrease the signal strength at frequencies close to, but not exactly at, the peak frequency. This poses a significant challenge because low-cost hardware components are often imprecise. The pass-band width is proportional to the ratio of the Tx wire resistance R_{coil} and inductance L_{coil} values:

$$\Delta f_{width} = \frac{1}{2\pi} \frac{R_{coil}}{L_{coil}}. \tag{6}$$

Because the CSM-EM instrument Tx coil has an inductance of $L_{coil} = 13.28$ mH and a resistance of $R_{coil} = 3.2$ Ohms, the RLC filter pass band is $\Delta f_{width} = 38.4$ Hz. While the 38.4 Hz bandwidth combined with a 1.57 kHz peak frequency, in theory, would prevent the 1.64 kHz RC oscillator signal from generating a sufficient Tx signal strength, we found that these components did produce high currents (>2.0 A) in the Tx coil. The calculated transmitter and receiver RLC gains are shown in Figure 5, indicating that a 1.64 kHz signal would still experience 10 dB transmitter signal gain when voltage is measured across the capacitor and a 15 dB signal gain over the receiver. While the full bandpass curve shown in 5 provides the most insight, equations 5 and 6 are useful for approximating the expected frequency when substituting electronics or making field modifications.
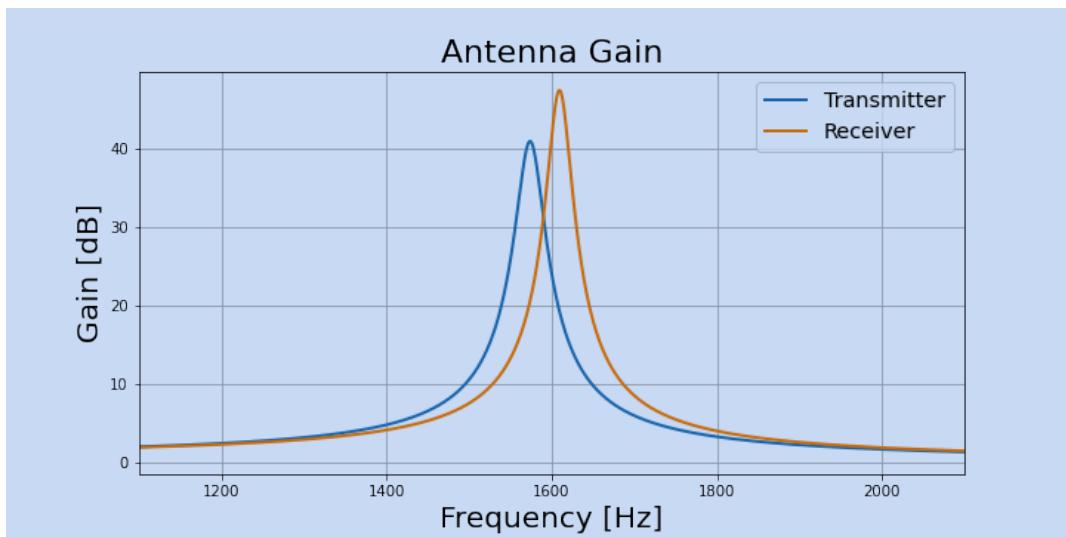
Figure 5. Response of the RLC circuit present in the transmitter unit, with inductance $L_{coil} = 13.28$ mH, capacitance $C_{coil} = 770$ nF, and resistance $R_{coil} = 3.2$ Ohms, and across the receiver unit, with inductance $L_{coil} = 12.7$ mH, capacitance $C_{coil} = 770$ nF, and resistance $R_{coil} = 2.7$ Ohms. The filtered signal can be measured over any of the components; however, both antennas measure the signal across the capacitor component. This is due to the small gain across the resistor component, and that the inductor in the RLC circuit is the antenna coil.

3.3 Receiver Design

The CSM-EM Rx antenna coil (Figure 6a) has the same dimensions, wire wraps, and wire gauge as the Tx antenna, although due to material heterogeneity the Rx coil resistance and inductance differ slightly from those of the Tx coil. The transmitted signal measured by the Rx unit is filtered through an RLC circuit that can be easily refitted to enable the Rx unit to pass different frequencies (bandpass curve examples is shown in Figure 5). The Rx coil has an intrinsic inductance $L_{coil} = 12.7$ mH, a resistance $R_{coil} = 2.7$ Ω, connected to a tuneable capacitor $C_{coil} = 770$ nF (Figure 6b). The resulting RLC filter has a calculated peak frequency of $f_{coil} = 1.61$ kHz and a pass-band width of $\Delta f_{width} = 33.8$ Hz due to the finite resistance of the Rx coil.

The filtered Rx signal (modeled in Figure 3a) is amplified using an inverting amplifier configuration powered by two 9 V batteries (see equation 4). Figure 6b illustrates the amplifier setup with a gain $G = 100$, set by $R = R_1$ and $R_f = R_F$. R_F is a variable resistor that allows the Rx gain to be changed without hardware refits. The op-amp gain increases the signal amplitude, allowing the user to observe minute signal changes on a readable scale. The signal gain shifts the Rx input signal up by two orders of magnitude, making any changes in the secondary field more easily observable on a 0.1 mV resolution multimeter (shown in Figure 3b). The filtered and amplified signals are measured as an RMS voltage by a DMM connected across the amplifier output.

3.4 Construction and Cost Considerations

Table 1 presents the itemized cost for all instrument components. The only tools and resources required for the build are a soldering iron, wire strippers, electrical tape and zip ties for structural integrity, and containers for electrical modules. The basic components used in the device build allow the user to substitute most components for those available, which has the potential to significantly lower costs. In most situations, the largest cost contributor - wire - can be re-purposed from other sources. While the OPA549 power amplifier unit can be built from scratch (Figure 4b), prefabricated boards likely provide greater Tx system durability, improve the modularity of the Tx design, and facilitate refits and repair.

4 Validation

The CSM-EM design goals specify that the system can function at frequencies and Tx-Rx offsets similar to those found in commercially available FDEM instruments. We used the Geonics EM-34 commercial Tx for validation and comparison purposes. The CSM-EM system was set to function at 1.67 kHz because of its size and compatibility with the Tx frequencies available on the EM-34. We ensured device functionality through laboratory tests designed to observe whether the CSM-EM could: (1) function at the desired frequencies; (2) emit stable Tx signals at amplitudes comparable to (or even greater than) the EM-34 Tx; and (3) detect conductive objects in a free-air environment at reasonable Tx-Rx offsets. After successfully validating functionality in the laboratory environment, the CSM-EM instrument has been tested in an outdoor setting by performing a survey over an area containing a known conductive anomaly.
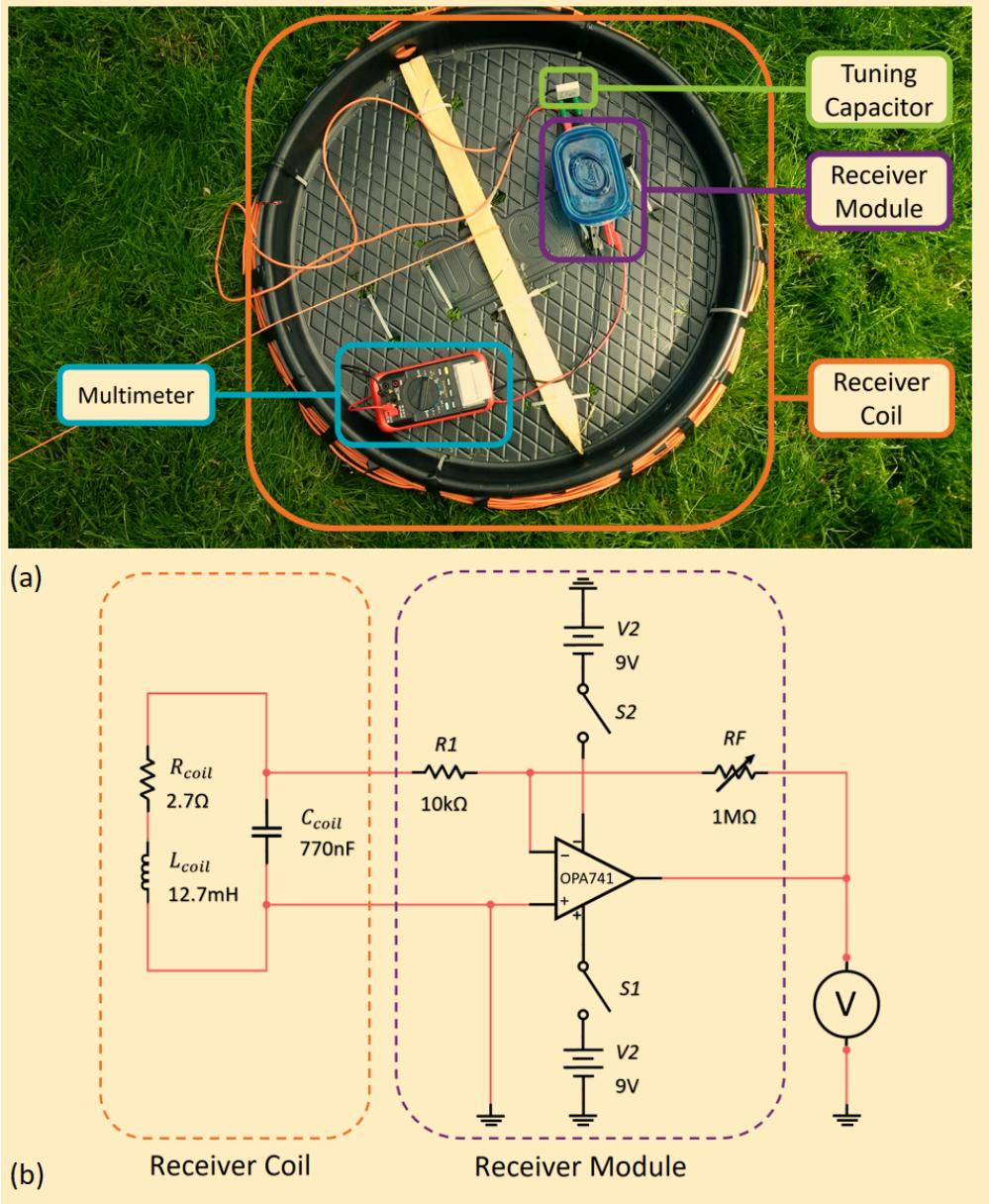
Figure 6. (a) Low-cost CSM-EM Rx system. The Rx coil (with attached tuning capacitor C_{coil}) acts as an RLC bandpass filter for a given frequency. The signal is passed through an inverting amplifier and an RMS voltage is measured by a DMM. (b) Low-cost CSM-EM Rx circuit diagram consisting of the Rx coil/tuning capacitor, an OPA741 inverting amplifier powered by two 9 V batteries, and a DMM. Two single pole switches are attached to the batteries to prevent unwanted power drain. The switches are not intended to function independently and can be replaced with one double pole switch; however, single pole switches are more widely available in most areas.

Table 1. Cost breakdown (in USD) for parts required to construct and operate the system. Note that this estimate assumes all products are bought new. Many components (especially wire) can be repurposed, allowing the system to be built at a lower overall cost.

Item	Cost (USD) / Unit	# of Units	Cost (USD) / Item
14 Gauge Wire	0.38 / m	400 m	152.00
Coil Frame	12.49	2	24.98
Breadboard, Wires, Banana Plugs	12.50	1	12.50
9 V Batteries	2.28	2	4.56
12 V Motorcycle Batteries	29.67	2	59.34
Switches	1.20	1	1.20
Electrical Components	4.97	1	4.97
741 Op-amp module	1.69	2	3.38
549 Power amp Module	40.00	1	40.00
Multimeters	29.97	2	59.94
		TOTAL	362.87

4.1   Laboratory Validation Tests

240   The first laboratory trial tested whether the CSM-EM Rx could detect a clear sinusoidal signal at a given frequency with a visible change in the signal amplitude when a conductor was placed nearby. For the trial, the Rx unit was placed in a near free-air environment (i.e., elevated on a mobile stand in the laboratory) at 10 m offset from the CSM-EM Tx. The Tx and Rx were set to function at 1.6 kHz. Figure 7 shows an oscilloscope display of the CSM-EM Rx signal with and without introducing a piece of sheet metal near the Rx. The Rx signal is a total field measurement; a superposition of the primary Tx

245   field and secondary fields generated from nearby conductive materials. As shown on the oscilloscope display, the Rx signal had a frequency of 1.67 kHz, with an RMS voltage of 271.9 mV, and a peak-to-peak (Pk-Pk) amplitude of 880.0 mV without the sheet metal present (brown curve). After the conductive body was placed between the CSM-EM Tx and the CSM-EM Rx, the signal amplitude decreased to less than half of the previous amplitude (yellow curve). This is because the secondary field created by conductive bodies destructively interferes with the primary signal, attenuating the total field measured by the Rx.

250   The RMS voltage was well within the resolution of a standard DMM. The initial test demonstrated that the Rx measured a stable field very close to the expected Tx frequency with an amplitude of several hundred mV, which is sufficiently observable on commercial DMMs. The test also indicates that the Rx responds to the destructive interference of secondary fields from the conductor, and that the amplitude change can be measured by a DMM as an RMS voltage.

Next, we tested the CSM-EM Tx unit for its ability to produce a stable signal of comparable strength to that of the EM-34

255   Tx unit. The system was set up in the same orientation as the former laboratory trial, but using an Rx gain of $G = 50$ at a 5 m Tx-Rx offset. The signal frequency in this trial was, as expected, nearly identical to the measured Rx signal from the previous
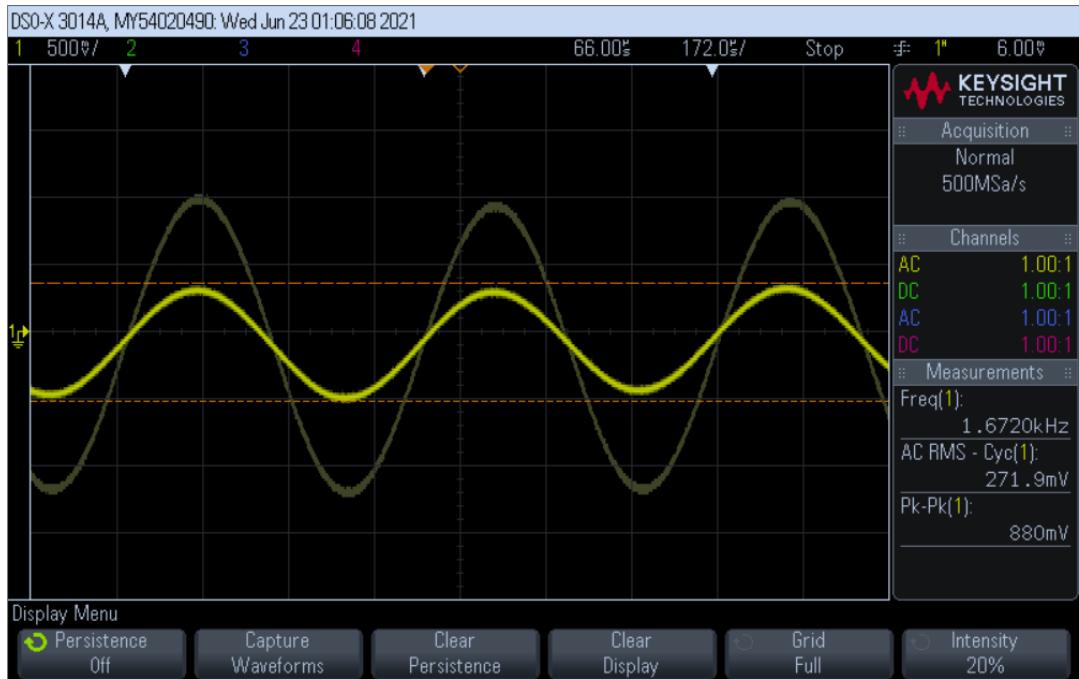
Figure 7. CSM-EM Rx signal measured on an oscilloscope using an Rx gain of $G = 100$ at a 10 m Tx-Rx offset with (yellow curve) and without (brown curve) introducing a piece of sheet metal near the Rx antenna. The signal with the sheet metal present is less than half the amplitude of that without metal present. The CSM-EM Tx generated the signal for both measurements.

trial (1.67 kHz). The RMS voltage was 3.42 V and the Pk-Pk amplitude was 9.9 V using the CSM-EM Tx and decreased to less than half the original amplitude when using the EM-34 Tx (yellow and brown curves in Figure 8, respectively), demonstrating that the CSM-EM Tx can produce a stable signal of comparable strength to that of the EM-34 Tx.

4.2 Field Validation Tests

Field validation testing involved completing an outdoor field survey over a shallow metallic target to test system sensitivity to a conductive object, and a qualitative Tx-Rx offset test. The field survey target was a manhole cover located at the surface in the outdoor Colorado School of Mines Geophysical Discovery Laboratory (GDL). The GDL is a flat sod-covered area with a thin layer of soil 0.5 m deep covering the surface. Backfill underneath the soil continues to a depth of 2 m, with thick shale units extending beyond the near-surface environment (Weimer, 1973). While the GDL can be considered geologically homogeneous for near-surface FDEM surveying applications, there is a large amount of electrical and plumbing infrastructure running throughout the area.

The survey consisted of two primary transects: (1) an east-west test line over the manhole cover, and (2) a parallel control line 4 m to the north of the test line (Figure 9a). The first trial used the EM-34 Tx with the CSM-EM Rx on the test line. The second trial combined the CSM-EM Tx and Rx units again on the test line. Finally, a third trial used the combined CSM-EM
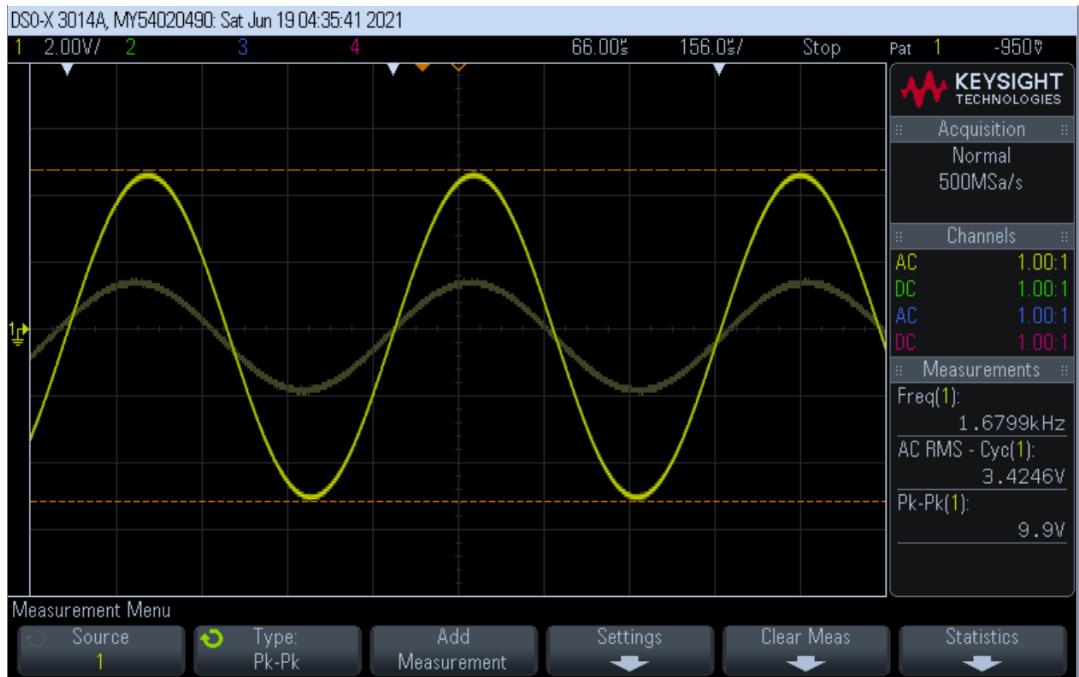
Figure 8. Low-cost CSM Rx signal (attached to oscilloscope) using an amplifier gain $G = 50$ at a 5 m Tx-Rx offset with the EM34 Tx (brown) and low-cost CSM-EM Tx (yellow). The amplitude of the signal received from the CSM-EM Tx is over twice that of the EM34 Tx.

Tx-Rx system but on the control line for calibration purposes. All Tx and Rx units were set to function at 1.6 kHz. The CSM-EM system for all trials was oriented along the two survey lines shown in Figure 9a with the Tx and Rx units separated by a fixed 5.0 m offset and starting at 25.0 m and 30.0 m easting, respectively. Measurements proceeded westward every 0.5 m and stopped when the Tx unit reached the 0.0 m easting coordinate. The CSM-EM Tx current and Rx RMS voltage were measured at each survey location. The current measurements ensured that the CSM-EM Tx unit exhibited a stable output throughout the survey. Figures 9b shows the current in the CSM-EM Tx over the test line (blue curve) and over the control line (green curve). Figure 9c presents RMS voltages measured by the CSM-EM Rx and shows a significant anomaly detected in both the EM-34 Tx and CSM-EM Tx trials (blue and orange curves, respectively) when either the Tx or the Rx passed directly over the target. In comparison, the CSM-EM control line data (green curve) exhibited no significant voltage drop.

The Tx-Rx offset testing was conducted in the GDL area away from the manhole cover, so that measurements could be made over a homogeneous subsurface. The CSM-EM Rx output was observed using an oscilloscope to gauge signal stability and a DMM to measure RMS voltage. Both the Tx and Rx devices were set to the same system parameters from the manhole cover field test. The CSM-EM Tx and the EM-34 Tx were tested separately, with the CSM-EM Rx in an HCP coupled orientation. Measurements took place at 5.0 m intervals. The EM-34 Tx paired with the CSM-EM Rx was tested starting at a Tx-Rx offset of 10.0 m, and continuing until the sinusoidal Rx signal was no longer resolvable on the oscilloscope. At 10.0 m the EM-34 Tx generated a clean signal with an RMS voltage of 150 mV, representing the total field strength. When the system was moved to
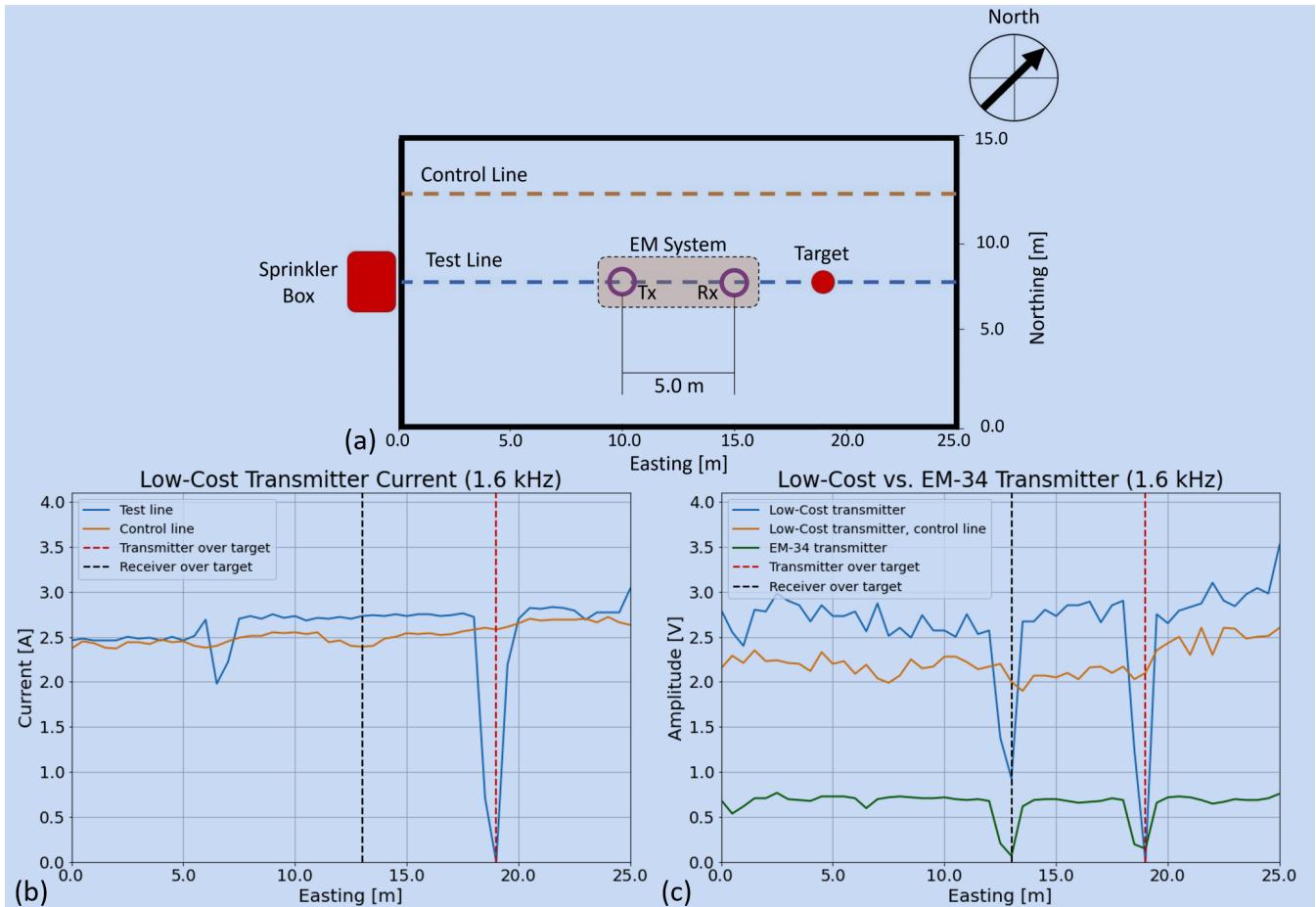
Figure 9. Geometry and results from the CSM-GDL field validation test using a 1.6 kHz Tx frequency. (a) Survey geometry showing the 0.75 m diameter manhole cover surface target located at 18.5 m easting on the test line. The control line is parallel to and 4 m north of the test line. The only other known nearby conductive body is a sprinkler box located close to the survey area. (b) The blue and orange curves show CSM-EM Tx current for the test and control lines, respectively. Along the test line, the Tx current dips when the antenna is directly over the manhole cover, as well as at 6.5-7.0 m easting. (c) The green and blue curves show the test line voltage data for the EM-34 Tx/CSM-EM Rx and the CSM-EM Tx/Rx combinations, respectively. Both curves show significant RMS voltage reductions when either the Tx or Rx passes over the target. The orange curve presents the control line data unaffected by the surface metal objects.

a 15.0 m offset, the Rx signal was very weak and had an RMS voltage of less than 60 mV. Because the CSM-EM Tx generated a larger signal in laboratory testing compared to the EM-34 Tx, the CSM-EM Tx coupled with the CSM-EM Rx was tested at larger offsets. At 20.0 m, the CSM-EM Tx generated a clean signal with a 130 mV RMS voltage, greater than the EM-34 Tx signal at 10.0 m offset from the CSM-EM Rx. At 25.0 m the CSM-EM Tx signal was still resolvable from the background noise, but the RMS voltage had dropped to 80 mV. At 30.0 m offset, the CSM-EM Tx signal was very weak, with an RMS

voltage of 60 mV. The offset test demonstrated that the CSM-EM Tx can produce a resolvable Rx signal at up to 25.0 m offset from the CSM-EM Rx unit.

5 Discussion

The CSM-EM system provided a variety of results from the engineering design process and the prototype validation tests. We initially designed the CSM-EM unit to be a tilt-angle EM system prototype (Frischknecht et al., 1991); however, early laboratory tests suggested that the Tx-Rx system was capable of conducting amplitude-based FDEM measurements when connected to a DMM measuring RMS voltage. While the laboratory and field test results present a proof of concept that the CSM-EM unit is capable of acquiring field-scale FDEM data, they also highlight several challenges experienced during CSM-EM data acquisition and analysis as well as opportunities for further research.

5.1 Proof-of-Concept

The CSM-EM unit can function at multiple frequencies at field-scale Tx-Rx offsets in an outdoor environment with a Tx signal strength comparable to that of the EM-34 Tx. The low-cost components required to construct the system are easily procurable; many parts also could be substituted to further decrease costs. The CSM-EM system is easy to adapt to a wide range of Tx-Rx frequencies with minor hardware changes, and can acquire data using a voltmeter. The system measurements can be connected to the analog-to-digital converter available on most microcontrollers (e.g., an Arduino Uno) for cost-effective, light-weight digital recording.

Field testing demonstrated that the complete CSM-EM system is sensitive to conductive objects and can produce similar amplitude-based data as the EM-34 Tx and CSM-EM Rx combination. The CSM-EM field trials show that the CSM-EM Tx produces larger Rx voltages and more prevalent anomalies than the commercial Tx. The CSM-EM Tx-Rx data have a variance of 0.118 V^2 over the test line, excluding data points over the target, and a variance of 0.029 V^2 over the control line. The data for the EM-34 Tx with the CSM-EM Rx have a variance of 0.011 V^2 over the test line, excluding data points over the target. The higher variance of the data measured using the CSM-EM Tx is significant enough to prevent the system from detecting small-scale near-surface resistivity changes, such as those caused by geological or fluid content variations. The CSM-EM Tx current (Figure 9c) exhibits similar trends to the CSM-EM Rx voltage when the Tx is directly over the manhole cover. The Tx current signal showed a variance of 0.012 A^2 over the control line and 0.036 A^2 over the test line. Along with higher data variance using the combined CSM-EM Tx/Rx, limited sampling of DMM readings make any kind of noise analyses difficult. Noise present in the CSM-EM field data indicates a lack of stability in the Rx signal and Tx current, which may be due to numerous factors including the lower build quality and reduced rigidity of the CSM-EM antennas, as well as the precision of the low-cost hardware (e.g., resistors, capacitors, inductors, repurposed wiring) used in the CSM-EM Tx build. The CSM-EM antennas were constructed around plastic liners and easily deform, which can affect the stability of signal transmission and could account for the greater observed variance in the Tx and Rx antennas. (The antennas were held flat in the HCP orientation to mitigate these effects during trials.) The quality and tolerances of the hardware used in the CSM-EM Tx unit may have

affected signal quality during testing. Issues with the hardware component connections could be mitigated by moving the components from a breadboard prototype a printed circuit board.

5.2 Future Development

The testing performed on the prototype CSM-EM system allows for several future developments. While the CSM-EM system resembles the EM-34 in size and shape, next-generation designs could use the same circuitry on a miniaturized scale to create a system more similar in size to lightweight single-operator EM systems. A miniaturized system would require less material (specifically antenna wire) and could function as a single rigid structure. Along with miniaturization, the Tx and Rx tuning capacitors and RC oscillator capacitors could be attached to rotary switches, which would permit the frequency range of the device to be changed without any hardware modifications.

Microcontroller inboard analog-to-digital converters are capable of voltage and current measurements when combined with basic electrical components (analogRead). This would allow for the CSM-EM system to digitally record measurements. Including a microcontroller module (e.g., an Arduino or Raspberry Pi) opens up the possibility of future CSM-EM versions to be operated remotely which, when combined with the system's potentially lightweight nature, creates opportunities for multi-Tx-Rx experiments.

By combining a more robust build with rapid autologger sampling, we aim to decrease noise during data acquisition and better analyze more densely recorded data through processing. With an improved system, we can determine whether the CSM-EM design is sensitive to small-scale resistivity variations due to geology or subsurface fluid content. We plan to perform more robust Tx/Rx offset tests with the future system to gauge performance improvements due to mechanical and electronic updates. Modifications are underway to perform phase-based measurements for a more direct comparison to commercial instruments. These mechanical and data-collection improvements will dictate future applications of the CSM-EM system in near-surface geophysical investigations.

6 Conclusions

The primary goals of this study were to design, build and validate a low-cost transmitter-receiver FDEM system for under US$400 that is of comparable size and signal transmission strength to commercial grade systems. The CSM-EM device costs US$363 for the current design when using all new parts and can detect conductive objects in a field environment using amplitude-based signal measurements. The modular design of the unit allows users to easily change components and to replace the DMM system with a microcontroller-based autologger. The CSM-EM functions at a variety of frequencies with minimal hardware adjustments and produces a stable signal of comparable strength to commercial systems (e.g., the Geonics EM-34 Tx). This proof-of-concept device provides a foundation for the future development and use of low-cost FDEM systems for near-surface geophysical and other related investigations.

Author contributions. GW, JC, JA, and AS designed, built, and tested the instrument. GW and JS were responsible for the preparing and

355 writing the manuscript with contributions from other co-authors. AS and JS were responsible for completing manuscript revisions.

Competing interests. The authors declare that they have no conflict of interest.

Acknowledgements. We would like to thank Dr. Reza Mir for valuable electronics advice during the construction of the CSM-EM system, and for reviewing this article. We would also like to thank Dr. James Clark for reviewing this article and for his valuable contributions to the development of low-cost geophysical instrumentation.

References

Ahmad, M. N., Iqbal, F., Maqbool, S., and Arshad, M. B.: Low-Cost Resistivity Meter for Groundwater Exploration Using High Voltage Experimentations, International Journal of Economic and Environmental Geology, 10, 35–39, https://doi.org/10.46660/ijeeg.vol10.iss3.2019.306, 2019.

Alexander, C. and Sadiku, M.: Fundamentals of Electric Circuits, McGraw-Hill Higher Education, Boston, 2007.

analogRead() function: Analogread(), https://www.arduino.cc/reference/en/language/functions/analog-io/analogread/.

Boaga, J.: The use of FDEM in hydrogeophysics: A review, Journal of Applied Geophysics, 139, 36–46, https://doi.org/https://doi.org/10.1016/j.jappgeo.2017.02.011, 2017.

Clark, J. A., Page, R. T., Franklin, R., Miller, N. M., and Morken, M. O.: Appropriate geophysics technology: Inexpensive instruments for water exploration at a local level in developing nations, pp. 171–181, https://doi.org/10.1130/2016.2520(16).

Dean, T., Nguyen, N., Kepic, A., Armitage, B., and Rossiter, H.: The democratization of seismic acquisition, in: SEG Technical Program Expanded Abstracts 2017, pp. 201–205, Society of Exploration Geophysicists, https://doi.org/10.1190/segam2017-17634981.1, 2017.

Fontaine, J. M., Percy, A., Oware, E. K., Bosompemaa, P., Gbedzi, V., and Lane, J. W.: Application of electromagnetic induction to develop a precision irrigation framework to facilitate smallholder dry season farming in the Nasia-Kparigu area of northern Ghana, in: SEG Technical Program Expanded Abstracts 2018, pp. 2491–2495, Society of Exploration Geophysicists, https://doi.org/10.1190/segam2018-2997867.1, 2018.

Frischknecht, F. C., Labson, V. F., Spies, B. R., and Anderson, W. L.: 3. Profiling Methods Using Small Sources, in: Electromagnetic Methods in Applied Geophysics, pp. 105–270, Society of Exploration Geophysicists, https://doi.org/10.1190/1.9781560802686.ch3, 1991.

Purcell, E. M.: Electricity and Magnetism, American Journal of Physics, 34 (9), 1966.

Schofield, I., Connors, M., and Russell, C. T.: NetPICOmag: A low-cost networked magnetometer and its applications, Earth, Planets and Space, 64 (3), 279–297, https://doi.org/10.5047/eps.2011.10.001, 2012.

Sea, C. D. and Ernenwein, E. G.: Frequency domain electromagnetic induction: an efficient method for investigating Fort Ancient village dynamics, Archaeological Prospection, 28 (1), 73–87, https://doi.org/10.1002/arp.1798, 2020.

Shahsavani, H.: Comparison of a low-cost magneto-inductive magnetometer with a proton magnetometer: A case study on the Galali iron ore deposit in western Iran, Near Surface Geophysics, 17 (1), 69–84, https://doi.org/10.1002/nsg.12026, 2018.

Shubitidze, F., Saparishvili, G., Barrowes, B., Shubitidze, T., and Prishvin, M.: ULEMA: Ultra-Light ElectroMagnetic Array system for UXO detection and classification, in: Symposium on the Application of Geophysics to Engineering and Environmental Problems 2021, p. 21, Symposium on the Application of Geophysics to Engineering and Environmental Problems Proceedings, https://doi.org/10.4133/sageep.33-012, 2021.

Sirota, D., Shragge, J., Krahenbuhl, R., Swidinsky, A., Yalo, N., and Bradford, J.: Development and validation of a low-cost direct current resistivity meter for humanitarian geophysics applications, Geophysics, 87 (1), WA1–WA14, https://doi.org/10.1190/geo2021-0058.1, 2021.

Soler-Llorens, J., Galiana-Merino, J., Nassim-Benabdeloued, B., Rosa-Cintas, S., Zamora, J., and Giner-Catulra, J.: Design and Implementation of an Arduino-Based Plug-and-Play Acquisition System for Seismic Noise Measurements, Electronics, 8 (9), 1035, 2019.

Ward, S. H. and Hohmann, G. W.: Electromagnetic Theory for Geophysical Applications, in: Electromagnetic Methods in Applied Geophysics, pp. 130–311, Society of Exploration Geophysicists, https://doi.org/10.1190/1.9781560802631.ch4, 1988.

Weimer, R.: A guide to uppermost Cretaceous stratigraphy, central Front Range, Colorado: deltaic sedimentation, growth faulting and early Laramide crustal movement, The Mountain Geologist, 1973.

White, E., Day-Lewis, F., Johnson, C., and Lane, J.: Application of frequency- and time-domain electromagnetic surveys to characterize hydrostratigraphy and landfill construction at the Amargosa Desert Research Site, Beatty, Nevada, in: Symposium on the Application of Geophysics to Engineering and Environmental Problems 2016, Society of Exploration Geophysicists and Environment and Engineering Geophysical Society, https://doi.org/10.4133/sageep.29-024, 2016.

Wilson, G., Young, C., Bernstein, B., and Shragge, J.: Developing low-cost open seismic nodal design for humanitarian groundwater investigations, in: Symposium on the Application of Geophysics to Engineering and Environmental Problems 2021, Society of Exploration Geophysicists and Environment and Engineering Geophysical Society, https://doi.org/10.4133/sageep.33-092, 2021.

400